Proceedings of the CAS–CERN Accelerator School: Free Electron Lasers and Energy Recovery Linacs, Hamburg, Germany, 31 May–10 June 2016, edited by R. Bailey, CERN Yellow Reports: School Proceedings, Vol. 1/2018, CERN-2018-001-SP (CERN, Geneva, 2018)

Electron Sources and Injection Systems

E. Chiadroni
National Laboratory of Frascati—INFN, Frascati, Italy

Abstract
High-brightness photo-injectors are mandatory for several applications, for instance plasma-based accelerators, linear colliders, novel radiation sources, such as free-electron lasers, terahertz radiation sources, and inverse Compton scattering sources; all require the production, acceleration, and manipulation of high-brightness electron beams.

Keywords
Brightness; photo-emission; photo-injectors.

1 Introduction

The physics and technology concerning the generation, manipulation, and transport of high-energy, high-quality electron beams are of crucial importance in different fields of science, e.g., for the R&D of future-generation light sources and novel plasma-based accelerators. Indeed, free-electron lasers (FELs) [1–4], energy-recovery linacs [5], light sources, inverse Compton scattering sources [6], and plasma-based accelerators [7] all demand high-brightness electron beams. The figure of merit of this electron source is the normalized brightness in 6D phase space. There is no unique definition of brightness, as the literature shows [8–13]; I choose in this regard the definition reported in Ref. [10] extended to the 6D phase space:

$$B_{6\mathrm{D}} = \frac{2I_{\mathrm{p}}}{\frac{\Delta\gamma}{\gamma}\varepsilon_{\mathrm{n}}^2} \,. \tag{1}$$

Efforts are made to maximize the brightness, thus minimizing the transverse projected emittance (ε_{n} is of the order of millimetre milliradians) and the energy spread ($\Delta\gamma/\gamma \sim 0.1\%$), or increasing the peak current (I_{p} of the order of kiloamps), which means shortening the electron bunch down to femtosecond-scale durations. In particular, in both energy-recovery linacs [5] and FELs [1–4], high time-resolution user experiments require extremely short X-ray pulses (shorter than femtoseconds), imposing the need for small and linear longitudinal emittances to allow for proper compression along the linac. Indeed, the exponential gain of self-amplified spontaneous emission FELs [14], as shown in Section 3, depends on the peak current and not on the charge, at the price of a reduced number of photons per pulse, with the advantage that a reduction of beam charge allows better control of the beam quality.

A great development of FEL user facilities has been driven by the advent of radio-frequency (RF) based photo-injectors, contributing to an improvement of the normalized transverse emittance of at least one order of magnitude [15].

In a photo-injector, electrons are emitted by a photocathode, located inside an RF cavity, illuminated by a laser pulse, so that the time structure of the electron beam can be controlled and shaped on a picosecond or subpicosecond time-scale via the laser pulse. This feature is one of the main advantages of laser-based RF injectors. Indeed, the space charge can be controlled by reducing the beam charge density, especially in the cathode region, where the beam energy is low, by working with larger laser spot sizes; space charge can also be controlled by increasing the bunch length, which, however, contributes to increasing the longitudinal emittance, requiring compression methods. In addition, to preserve the brightness, the emitted electrons must be rapidly accelerated to relativistic energies, thus damping the space-charge forces, which scale as $1/\gamma^2$, and resulting in a partial mitigation of the emittance growth. At this regard, RF fields allow for large, from ≈40 to ≈130 MV/ m, electric fields at the cathode surface;

2519-8041 – © CERN, 2018. Published by CERN under the Creative Common Attribution CC BY 4.0 Licence.

https://doi.org/10.23730/CYRSP-2018-001.401

therefore, a laser-assisted RF gun is the preferable choice because of the high peak field, $\sim 10^2$ MV/ m, and the possibility of shaping the 6D electron-beam phase spaces by acting on the laser pulse distributions, both transverse and longitudinal. In addition, the generation of longitudinally modulated electron bunches directly at the cathode by means of a *comb-like* laser profile [16] is advantageous for the successful development of new classes of application, e.g., plasma wakefield accelerators [17], high-power narrow-band coherent terahertz sources [18], and two-colour FEL radiation [19–21].

In this report, I will overview electron injectors, highlighting the physics of the emission process and focusing on the beam dynamics in normal conducting RF guns. An extensive and detailed study can be found in Ref. [22]. In addition, I will introduce emittance compensation techniques to limit emittance growth at the end of the injector, integrated in a RF-based longitudinal compression method.

2 Definition of brightness

In 1939, Von Borries and Ruska, who were awarded the Nobel Prize in 1986 for the invention of the electronic microscope [23], introduced the concept of beam brightness as

$$B_{\mathrm{microscope}} = \frac{I}{A\Omega} = \frac{Ne}{\pi r^2 \pi \alpha^2 \Delta t} \approx \mathrm{constant}\ , \tag{2}$$

where $Ne/\Delta t$ is the electron current density escaping from the cathode surface with area $A = \pi r^2$, $\Omega = \pi\alpha^2$ is the solid angle in which electrons are emitted, and Δt is the time interval. This quantity is practically constant in the microscope column: therefore, the smaller the spot size, the larger the divergence. The brightness is extremely important because it defines the quality of the source and sets the kind of experiments that can be done. Indeed, for imaging applications, the larger the number of electrons, the better the contrast; spatial resolution and coherence are enhanced by a small area and a collimated beam, i.e., small angles α, while temporal resolution is improved by short pulses. The definition in Eq. (2) still holds nowadays in the field of electron microscopy, with peak values of $B_{\mathrm{microscope}}$ up to 10^{13} A/ m^2/ sr.

In analogy with the electron microscope brightness, it is convenient to define the 6D electron-beam brightness to compare and describe electron sources, as the number of electrons per unit volume $V_{6\mathrm{D}}$ occupied by the beam in 6D phase space, i.e., transverse (x, p_x, y, p_y), longitudinal (z, p_z), and proportional to the product of the three normalized emittances:

$$B_{6\mathrm{D}} = \frac{Ne}{V_{6\mathrm{D}}} \propto \frac{Ne}{\varepsilon_{\mathrm{n}x}\varepsilon_{\mathrm{n}y}\varepsilon_{\mathrm{n}z}}\ . \tag{3}$$

Liouville's theorem states that the phase space volume, bounded by a closed, arbitrary surface in the phase space, is constant, provided that only conservative forces act on the particles. As long as the particle dynamics in the beamline elements (transport optics, accelerating sections, etc.) can be described by Hamiltonian functions, that is, neither particle–particle collisions nor stochastic processes are considered, the phase space density will stay constant throughout the accelerator.

If we write the longitudinal emittance explicitly, in terms of energy spread, σ_γ, and bunch duration, σ_t, then the physical meaning of the 6D brightness is clear,

$$B_{6\mathrm{D}} \propto \frac{Ne}{\varepsilon_{\mathrm{n}x}\varepsilon_{\mathrm{n}y}\sigma_t\sigma_\gamma}\ : \tag{4}$$

a large number of quasi-monochromatic electrons, concentrated in very short bunches, with small transverse size and divergence, which means small transverse emittance. For a fixed charge/bunch this translates to preserving the transverse emittance and increasing the final current by reducing the bunch length. In numbers, for typical electron-beam parameters ($N \approx 10^9$, $\sigma_\gamma \approx 10^{-3}$, $\varepsilon_{\mathrm{n}} \approx$1 mm mrad, $\sigma_t < 1$ ps), the 6D brightness is of the order of 10^{15} A/ m^2.

The maximum brightness theoretically achievable by an electron beam is set by the Heisenberg uncertainty principle with one electron in each elementary quantum h^3 unit of phase space volume:

$$B_{\mathrm{quantum}} = \frac{2e}{h^3}(m_0c^2)^3 = \frac{2e}{\lambda_{\mathrm{c}}^3} \,, \tag{5}$$

with h the Planck constant, e the elementary charge, m_0 the particle mass, and c the speed of light; λ_{c} is the Compton wavelength, which for electrons is 2.426 pm. Replacing numbers in Eq. (5), $B_{\mathrm{quantum}} \approx 10^{25}$ A/ m^2, being 10 orders of magnitude larger than typical 6D brightnesses in photo-injectors.

The maximum brightness practically achievable is limited by the degeneracy parameter δ, which represents the number of particles per elementary volume of the phase space: $B = \delta B_{\mathrm{quantum}}$. In principle, assuming the photo-emission process by metal photocathodes, we expect a peak brightness approaching the quantum limit, since the degeneracy factor inside a metal is $\sim$1. However, in practice, we have 10 orders of magnitude less. Electron emission mechanisms and Coulomb interactions play a crucial role in this severe reduction of beam brightness [24].

The brightness generated at the electron source represents the ultimate value. Possible sources of emittance growth are:

- non-linear space-charge forces;
- non-linear forces from electromagnetic components, e.g., due to wakefields;
- synchrotron radiation emission (in magnetic compressors).

Sources of emittance degradation need to be kept under control, keeping in mind that the final beam quality is set by the linac and ultimately by its injector and electron source; therefore, a careful definition and specific requirements for both electron sources and injection systems are mandatory.

3 Applications of high-brightness electron beams

The great improvement of the characteristics of electron injectors started in the 1960s with thermionic guns [25]. Thermionic RF guns employ cathodes that must be heated to allow emission of electrons. Commonly used cathode materials are LaB_6, CeB_6, and BaO, with typical operating temperatures of the order of 1000 °C. The disadvantages of thermionic guns lie in the fact that emission occurs throughout the RF accelerating phase and during every RF period, resulting in a beam with large momentum and time spread. However, the high stability is the main advantage.

In 1985, the need for fast and precise control of the electron pulse shape led to the first use of photocathode RF guns because of the impressive reduction in transverse emittance, more than a factor of ten [15], promoted by the ability to shape drive laser pulses and rapidly accelerate electrons from rest to relativistic energies.

Starting from the first working prototype of an RF gun [26, 27], RF photo-injectors are nowadays routinely exploited as electron sources for FEL user facilities [1–4] and multidisciplinary test facilities, such as SPARC_LAB [28]. Radio-frequency photo-injectors are also fundamental for the successful development of plasma-based accelerators where external injection schemes are considered, i.e., particle-beam-driven [17] and laser-driven [29] plasma wakefield accelerators, since the ultimate beam brightness and its stability and reproducibility are strongly influenced by the RF-generated electron beam.

The main supporter for the development of high-brightness injectors is represented by X-ray free-electron lasers [30]. In particular, for FEL applications, the 5D brightness is often used to compare electron sources:

$$B_{5\mathrm{D}} = \frac{2I_{\mathrm{p}}}{\varepsilon_{\mathrm{n}x}\varepsilon_{\mathrm{n}y}} = \frac{2I_{\mathrm{p}}}{(\beta\gamma)^2\varepsilon_x\varepsilon_y} \,, \tag{6}$$

and is the relativistic analogue of the microscopic brightness.

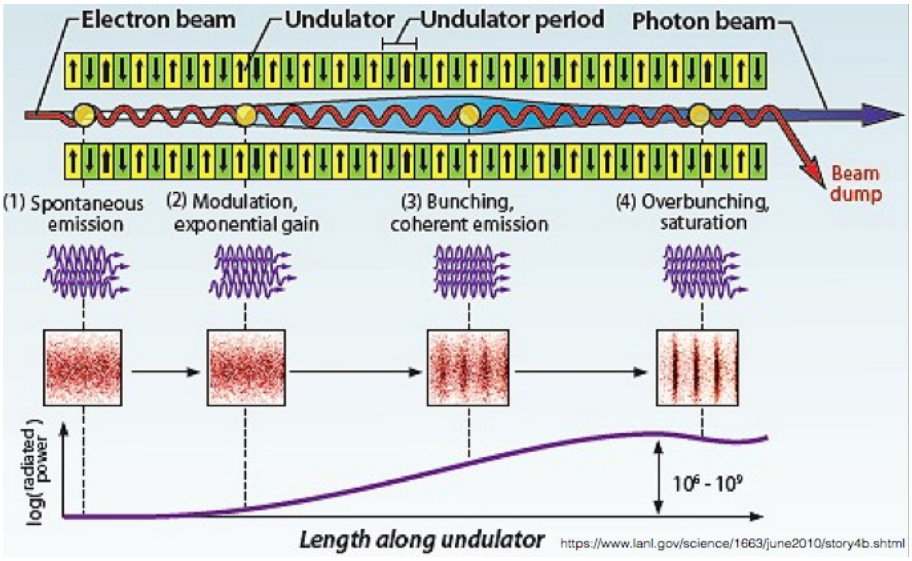

Fig. 1: Top: propagation of electron beam in undulator module. Middle: evolution of electron bunching along undulator. Bottom: exponential increase of FEL radiation power along the undulator.

In an electron beam entering a magnetic undulator, electrons start to oscillate with period λ_u and emit spontaneous radiation as synchrotron radiation because of the oscillating trajectory. They start to lose energy in favour of the radiation and since the trajectory in the undulator is energy-dependent, while propagating they start to bunch, which means that they start to modulate themselves longitudinally, as shown in Fig. 1.

Emission begins to be coherent and the radiation wavelength is set by the resonance condition:

$$\lambda_\mathrm{r} = \frac{\lambda_\mathrm{u}}{2\gamma^2}\left(1 + \frac{K^2}{2} + \gamma^2\theta^2\right) , \tag{7}$$

where γ is the electron-beam Lorentz factor, $K = (eB_0\lambda_\mathrm{u})/(2\pi m_0 c)$ is the undulator parameter, which defines the oscillation amplitude, and θ is the emitted angle with respect to the axis. B_0 is the maximum amplitude of the magnetic field and m_0 is the electron mass, thus K is a measure of the on-axis undulator magnetic field once the undulator period is fixed.

Because of the longitudinal modulation of the electrons in slices, the radiated power along the undulator increases exponentially as a function of gain length, which, in 1D FEL theory, is defined as

$$L_\mathrm{g} = \frac{\lambda_\mathrm{u}}{4\pi\rho\sqrt{3}} , \tag{8}$$

assuming a mono-energetic beam and neglecting space-charge forces. L_g represents the length necessary for the radiation field to be increased by e, Napier's constant; therefore it is an indication of how long the undulator chain should be in order to reach saturation. Beginning from shot noise, it typically takes a self-amplified spontaneous emission FEL about 20 L_g to reach saturation. The gain length is related to the beam brightness through the Pierce parameter, ρ,

$$\rho = \frac{1}{2\gamma}\left[\frac{I_\mathrm{p}}{I_\mathrm{A}}\left(\frac{\lambda_\mathrm{u} K[JJ]}{\sqrt{8}\pi\sigma_x}\right)^2\right]^{1/3} , \tag{9}$$

which scales with the peak current as $\rho \propto I_\mathrm{p}^{1/3}$, resulting in $L_\mathrm{g} \propto B_\mathrm{5D}^{-1/3}$; $I_\mathrm{A} = 4\pi\varepsilon_0\frac{m_0 c^3}{e} \approx 17$ kA is the Álfven current for an electron, $[JJ]$ is the Bessel function coupling factor depending on the undulator,[1]

[1] $[JJ]$=1 for helical undulators and $[JJ] = J_0\left(\frac{K^2}{4+2K^2}\right) - J_1\left(\frac{K^2}{4+2K^2}\right)$ for planar ones.

and σ_x is the r.m.s. electron transverse beam size in the undulator. I_A represents a limit on the amount of charge that can be transported. Physically, the beam self-magnetic field becomes sufficiently strong to stop the propagation of electrons, whose trajectories reverse in direction, so that most of the electrons are reflected back [31, 32].

The Pierce parameter, also called the universal FEL parameter, gives an indication of the gain of the FEL and the speed of the bunching process; typically for kiloamp-current beams, $\rho \sim 10^{-3}$ to 10^{-4} in the VUV/X-ray regime. In practice, $\rho \sim 1/N_{\mathrm{u}}$, where N_{u} is the number of undulator periods electrons must travel to increase the FEL power by 2e times. Indeed, the saturation power of the self-amplified spontaneous emission FEL radiation is $P_{\mathrm{sat}} = P_{\mathrm{in}}\mathrm{e}^{z/L_{\mathrm{g}}}$, with P_{in} the initial beam power; $P_{\mathrm{in}} = \rho I_{\mathrm{p}} E_{\mathrm{beam}}$.

In general, because of the finite energy spread and non-negligible space-charge effects, the exponential gain might weaken, resulting in an increased undulator length to preserve the FEL gain and aim at laser saturation. Therefore, the electron-beam brightness has to be extremely high in order to obtain a relatively short FEL gain length.

In addition, the brightness plays an important role on the efficiency of the FEL process and on its spectral characteristics. Indeed, to ensure coupling between the electron beam and the radiation it emits, the matching condition for transverse emittance has to be satisfied ($\varepsilon_{\mathrm{n}} < \gamma\lambda_{\mathrm{r}}/4\pi$). Concerning the energy spread, the matching condition requires $\sigma_\delta < \rho \approx 10^{-3}$, which defines the radiation bandwidth $\Delta\omega/\omega \approx 1/N_{\mathrm{u}} \approx \rho$.

Beyond X-ray FELs, high-brightness electron beams are needed for several other applications: for instance, high-power FELs, either for soft X-rays or IR, energy-recovery linacs, and linac-based terahertz sources all demand average currents of the order of milliamps, repetition rates of the order of megahertz, and low emittance. In addition, terahertz sources require ultrashort electron bunches, of the order of 10–100 fs, to extend the frequency spectrum up to several terahertz. Concerning the development of radiation sources, high-brightness electron beams are also fundamental in the success of γ-ray sources, such as inverse Thomson or Compton scattering [6]. A relativistic electron beam collides head-on with an ultrafast laser to produce scattered photons upshifted in energy in a $1/\gamma$ forward cone angle. The high-charge beam increases the X-ray yield, while short bunches allow for ultrafast X-rays. Both small emittance, which enables focusing to a micrometre-scale spot size, and low energy spread contribute to narrow the radiation bandwidth [33].

High-brightness photo-injectors are fundamental for the successful development of plasma-based accelerators. In particular, in particle-beam-driven plasma wakefield accelerators, the high-gradient wakefield is driven by an intense, high-energy charged-particle beam, named the driver beam, as it passes through the plasma. The space-charge forces of the electron bunch blow out the plasma electrons, which rush back in and overshoot, setting up a plasma density oscillation at a frequency $\omega_{\mathrm{p}} = \sqrt{(n_0 e^2)/(\varepsilon_0 m_0)}$, which depends on the plasma density n_0. A second, appropriately phased accelerating beam, named the witness beam, and containing fewer particles than the drive beam, is then accelerated by the wake. The energy transfer from the drive bunch to the plasma is optimized by maximizing the transformer ratio $R = |E_{+,\max}/E_{-,\max}|$, defined as the ratio between the maximum accelerating field behind the drive bunch, $E_{+,\max}$, where the particles of the witness bunch can be placed, and the maximum decelerating field within the drive bunch, $E_{-,\max}$. R quantifies the energy gain of a witness bunch placed at the accelerating phase. To accelerate high-brightness electron beams, both driver and witness bunches must be focused to a size of a few micrometres, as requested by the transverse matching condition at the plasma entrance, i.e.,

$$\sigma_{\perp}^{\mathrm{matching}} = \left(\frac{2}{\gamma}\right)^{1/4} \sqrt{\frac{\varepsilon_x}{k_{\mathrm{p}}}}\,, \tag{10}$$

with $k_{\mathrm{p}} = 2\pi/\lambda_{\mathrm{p}}$ the plasma wave number, λ_{p} the plasma wavelength, and ε_x the transverse emittance; therefore, the lower the emittance the smaller the beam transverse size. In addition, the great flexibil-

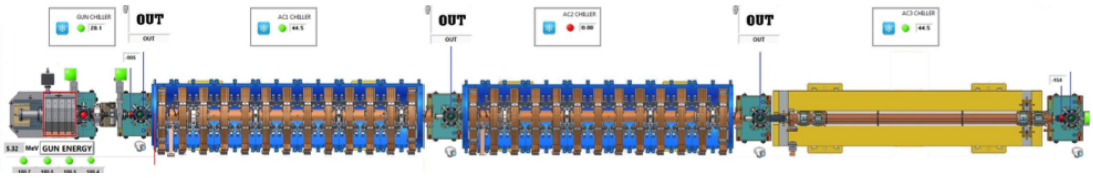

Fig. 2: Layout of SPARC_LAB photo-injector: a copper cathode, illuminated by UV laser pulses and embedded in a 1.6-cell standing wave S-band RF gun, generates a 5.6 MeV electron beam. A four-coil solenoid magnet focuses and matches the beam into three S-band travelling wave accelerating structures to boost the energy to 180 MeV. The first two accelerating structures are embedded by multicoil solenoid magnets to provide additional focusing when the first section is used as a RF compressor in the so-called velocity-bunching regime.

ity of photo-injectors to shape and manipulate the longitudinal phase space allows for resonant plasma wakefield acceleration driven by multibunch trains to increase the transformer ratio [34].

4 Photo-injector theory

An electron injector is the overall system from the electron source, the cathode, up to the place where electrons have energies where space-charge forces, which scale as $1/\gamma^2$, can be considered negligible. Therefore, the beam evolution is no longer space-charge dominated.

There are, at present, three broadly identifiable cathode technologies for electron-beam sources and two main accelerator technologies used to perform the initial acceleration of the beam from those cathodes, i.e., normal conducting (LCLS, FERMI, SPARC_LAB) and superconducting (FLASH, XFEL). Most injector systems use photocathodes; one exception is the SACLA XFEL [35, 36], which successfully uses a thermionic cathode.

In this review, I will focus on the experience at SPARC_LAB which, being an R&D facility on high-brightness photo-injectors, is paradigmatic for describing electron-beam generation, manipulation, and acceleration. I recommend Ref. [22] for a more complete treatment of electron sources and injection systems and Refs. [30, 37] for FEL physics and direct experience at user facilities.

The typical layout of an electron photo-injector is reported in Fig. 2. A photo-injector consists of a laser-generated source, followed by an electron-beam optical system, which preserves and matches the beam into a high-energy accelerator. A photocathode, embedded in a RF gun, releases picosecond or subpicosecond electron bunches when irradiated by laser pulses of given wavelength, depending on the cathode material. The high electric fields produced by the RF gun are necessary both to extract the high current and to minimize the effects of space charge on emittance growth. Since the RF gun acts as a strong defocusing lens, a solenoid magnet is needed to focus the divergent beam, preventing particle losses, and to properly match the electron beam to the accelerating cavities, minimizing emittance growth at the end of the accelerating chain (i.e., the linac exit).

A typical photocathode RF system depicts a $1\frac{1}{2}$-cell with a cathode embedded in the half cell. The cathode might be either metal or semiconductor depending mainly on applications: in the low-charge regime, the ultimate brightness performance of the linac is set by the cathode intrinsic emittance, while for high-repetition-rate photon sources, high-quantum-efficiency photocathodes are required.

The elements that constitute a photo-injector are highlighted in the following sub-sections.

4.1 Photocathode emission

The emission process determines the fundamental lower limit of the beam emittance, called the intrinsic emittance, which represents the minimum emittance achievable and depends on the emission mechanism, i.e.:

– thermionic emission [25];

– field emission [38];
– photo-electric emission [39].

The ideal cathode should have low intrinsic emittance, since this limits the maximum achievable brightness; high quantum efficiency, to reduce the laser load; long lifetime, uniform emission, since hot spots on the cathode and surface roughness contribute to emittance growth [40]; and fast response, which allows transverse and longitudinal electron-beam manipulation by properly shaping the laser pulse. At present, there is no cathode that meets all these criteria. Semiconductor photocathodes, for instance, are the best choice for high quantum efficiency and low emittance, while metallic photocathodes are chosen because of their fast temporal response, long operational lifetime, and high vacuum compatibility. An extensive and detailed study is reported in Ref. [22].

To understand the mechanism of electron emission from a cathode material, it is important to identify the fields and the potentials at the cathode surface and close to it. The electric potential energy as a function of the distance, x, from the cathode is given as

$$e\Phi = e\Phi_{\mathrm{work}} - \frac{e^2}{16\pi\varepsilon_0 x} - eE_0 x \,, \tag{11}$$

and is the sum of the work function energy, $e\Phi_{\mathrm{work}}$, which represents the work necessary to separate a charge from its image within the material and depends on the material, the image charge potential, $-e^2/(16\pi\varepsilon_0 x)$, and the potential corresponding to a constant electric field normal to the surface, E_0. Electrons with energies greater than the work function can escape the barrier, while those with lower energies can tunnel through it. In the case of thermionic and photo-electric emission, electrons are excited above the barrier to escape, while in the field emission the barrier height is lowered by the external field to encourage tunnelling. The reduction of the barrier by the applied field is called the Schottky effect and plays a central role in all emission processes, especially field emission [41].

Photo-electric emission is well described by Spicer's three-step model.

1. Photon energy absorption by the electron:
   (a) the optical skin depth depends on photon wavelength (∼14 nm for UV light on copper); reflectivity, and absorption as the photons travel into the cathode.
2. Electron transport to the surface through:
   (a) electron–electron scattering, dominant for metals;
   (b) electron–phonon scattering, dominant for semiconductors;
   (c) angular cone of escaping electrons.
3. Electron escape through the barrier:
   (a) Schottky effect and abrupt change in electron angle across the metal–vacuum interface; classical escape over the barrier due to the applied field.

Combining the three steps, the quantum efficiency can be expressed in terms of the probabilities of these processes occurring:

$$\mathrm{QE}(\omega) = [1 - R(\omega)] F_{e-e}(\omega) \frac{\int_{E_\mathrm{F}+\Phi_\mathrm{eff}-\hbar\omega}^{E_\mathrm{F}} \mathrm{d}E \int_{\sqrt{\frac{E_\mathrm{F}+\Phi_\mathrm{eff}}{E+\hbar\omega}}}^{1} \mathrm{d}(\cos\vartheta) \int_0^{2\pi} \mathrm{d}\phi}{\int_{E_\mathrm{F}-\hbar\omega}^{E_\mathrm{F}} \mathrm{d}E \int_{-1}^{1} \mathrm{d}(\cos\vartheta) \int_0^{2\pi} \mathrm{d}\phi} \,. \tag{12}$$

The first factor represents the probability of a photon being absorbed by the metal, which depends on the optical reflectivity: $R(\omega) \sim 40\%$ for metals and $R(\omega) \sim 10\%$ for semiconductors; the second factor, $F_{e-e}(\omega)$, is the probability that an electron will reach the surface without scattering with another electron, which for metals is 20%; the third factor is the probability that an electron will be excited into a state with sufficient perpendicular momentum to escape the material, over the barrier:

– occupied states with enough energy to escape, ∼0.04;
– electrons with angle within the max angle for escape, ∼0.01;
– azimuthally isotropic emission, ∼1.

The total energy of an electron inside the cathode after absorption of the photon is $E + \hbar\omega$, therefore the total momentum inside and outside is

$$p_{\mathrm{total,in}} = \sqrt{2m_0(E + \hbar\omega)}\,, \qquad p_{\mathrm{total,out}} = \sqrt{2m_0(E + \hbar\omega - \Phi_{\mathrm{eff}} - E_{\mathrm{F}})}\,, \tag{13}$$

where E_{F} is the Fermi level. The electron within the material, approaching the boundary surface, needs to have sufficient longitudinal momentum to escape, i.e.,

$$\sqrt{2m_0(E + \hbar\omega)}\cos\vartheta_{\mathrm{in}} \geq \sqrt{2m_0(\Phi_{\mathrm{eff}} + E_{\mathrm{F}})}\,, \tag{14}$$

where $\cos\vartheta_{\mathrm{max,in}} = \sqrt{\Phi_{\mathrm{eff}} + E_{\mathrm{F}}/E + \hbar\omega}$. In analogy to photons, electrons refract as they transit the cathode interface, as a consequence of the boundary condition requiring conservation of transverse momentum across the metal–vacuum transition, $p_{x,\mathrm{in}} = p_{x,\mathrm{out}}$ and $p_{\mathrm{total,in}}\sin\vartheta_{\mathrm{in}} = p_{\mathrm{total,out}}\sin\vartheta_{\mathrm{out}}$.

Combining the probabilities, it is possible to evaluate the nominal quantum efficiency for a copper photocathode, i.e., $\mathrm{QE} \sim 5 \times 10^{-5}$ [42]. As a rule of thumb, the quantum efficiency is given by $\mathrm{QE} = N_{\mathrm{e}}/N_{\mathrm{ph}} = (h\nu[\mathrm{eV}]/E_{\mathrm{laser}}[\mathrm{J}])Q[\mathrm{C}]$; therefore, to extract 1 nC of charge from a copper photocathode, a UV (266 nm) laser energy of the order of 100 µJ is required.

The linear dependence between the number of emitted electrons and the incident number of photons holds until a critical intensity of the laser pulse is reached. Indeed, for higher laser intensities, electrons will be emitted even for photon energies below the work function. In this case, $n > 1$ photons have to be absorbed at the same time in order to promote an electron to an unbound state with enough kinetic energy to escape the material, the scaling of the emitted charge being the nth power of the laser intensity. Taking advantage of the multiphoton emission process, an IR-wavelength laser incident on a metal cathode might also be used for electron-beam generation, in particular, when ultrashort pulses are required [43].

Depending on the application, the cathode choice must be driven not only by the quantum efficiency, but also by the intrinsic emittance, which represents the ultimate achievable emittance.

The intrinsic emittance is a feature of the emission process. To derive it, the definition of r.m.s. emittance, $\varepsilon_{\mathrm{n},x} = \beta\gamma\sqrt{\langle x^2\rangle\langle x'^2\rangle - \langle xx'\rangle^2}$, can be used, observing that the correlation term, $\langle xx'\rangle^2$, is null out of the cathode. Therefore,

$$\varepsilon_{\mathrm{n},x} = \sigma_x \frac{\sqrt{\langle p_x^2\rangle}}{m_0 c} \tag{15}$$

is a function of the laser pulse spot size, σ_x, and the transverse momentum, p_x, as determined by the emission process.

By calculating the IInd-order transverse momentum of the electron distribution function, we get the photo-electric normalized emittance as

$$\varepsilon_{\mathrm{n},x}^{\mathrm{intrinsic}} = \sigma_x \sqrt{\frac{\hbar\omega - \Phi_{\mathrm{eff}}}{3m_0c^2}}\,. \tag{16}$$

Therefore, to minimize the intrinsic emittance, one has to reduce the energy difference, $\Delta = \hbar\omega - \Phi_{\mathrm{eff}}$, between the energy of the incident photons and the effective work function of the material. However, since the quantum efficiency is proportional to Δ^2, a low intrinsic emittance also results in a low quantum efficiency.

4.1.1 Space-charge limit emittance

As emitted electrons come out from the cathode surface, they create their own electric field and start to fill the entire region, which can be represented as two parallel plates, i.e., cathode and anode, placed at a distance d, with an applied field or bias potential, V. In the beam tail, the beam self-field is opposed to the applied field and increases with the extracted charge. The effective potential is then distorted, creating asymmetries in the tail and setting a maximum extractable current in the steady-state regime. The maximum current density extractable is given, by solving the Poisson equation, by the Child–Langmuir law [44], which expresses how the steady-state current varies with both the gap distance, d, and the bias potential of the parallel plates, V, that schematize the RF gun:

$$j_{\mathrm{CL,1D}} = \frac{4\varepsilon_0}{9}\sqrt{\frac{2e}{m_0}}\frac{V^{3/2}}{d^2} \,. \tag{17}$$

This formula has been derived by assuming an infinitely wide beam in the transverse dimensions (i.e., 1D approximation) that completely fills the accelerating gap. However, in state-of-art photo-injectors, the initial electron-beam pulse length is always much smaller than the accelerating gap; in addition, the laser spot size on the cathode is usually smaller than millimetres in diameter to decrease the cathode emittance contribution, therefore the 1D Child–Langmuir formula is no longer valid. Indeed, to describe a real case, it is convenient to introduce the aspect ratio, i.e., the ratio between the beam radius and its length, to define pancake-like ($\gg$1) and cigar-like ($\ll$1) beams. In the case of pancake-like beams, the maximum surface charge density is set by the cathode extraction field, while in cigar-like beams only a small part of the beam contributes to the space-charge field and a higher charge can be extracted. The space-charge limit is reached when the space-charge field equals the applied, external field, E_0, and electron emission saturates. At the space-charge limit, the emitted charge saturates and the emission becomes constant. In the RF gun, the signature for the observation of the space-charge limit is the non-linear dependence of the charge on the laser energy.

The space-charge limit sets a minimum value for the beam emittance, once the applied field at the cathode, E_a, and the required charge, Q_{bunch}, are known. Indeed, for a cylindrical uniformly filled beam with radius R, the r.m.s. size is $\sigma_x = R/2 = \sqrt{(Q_{\mathrm{bunch}})/(4\pi\varepsilon_0 E_{\mathrm{a}})}$; therefore, substituting it in the normalized intrinsic emittance for photo-electric emission (Eq. (16)), we get

$$\varepsilon^{\mathrm{SCL}} = \sqrt{\frac{Q_{\mathrm{bunch}}(\hbar\omega - \Phi_{\mathrm{eff}})}{4\pi\varepsilon_0 m_0 c^2 E_{\mathrm{a}}}} \,. \tag{18}$$

The dependencies of the space-charge limit emittance on both the applied field and the charge are reported in Fig. 3(a) and (b), respectively. The space-charge limit emittance sets a maximum transverse brightness, which in the case of pancake-like beams does not depend on the charge, but only on the applied RF field and on the emission process:

$$B_\perp = \frac{N}{\varepsilon_{\mathrm{n}x}\varepsilon_{\mathrm{n}y}} \qquad \rightarrow \qquad B_\perp^{\max} = 4\pi\varepsilon_0 \frac{E_{\mathrm{a}}}{e}\frac{m_0 c^2}{\hbar\omega - \Phi_{\mathrm{eff}}} \,. \tag{19}$$

4.2 RF gun

Once the electrons are out of the cathode surface, they have to be promptly accelerated to keep under control the emittance growth driven by space-charge forces. For this purpose, the relevant modes are those with large longitudinal electric fields E_z, since the energy transfer occurs when the particle's velocity is parallel to the electric field:

$$\frac{\mathrm{d}U}{\mathrm{d}t} = Q\vec{v}\cdot\vec{E} \,. \tag{20}$$

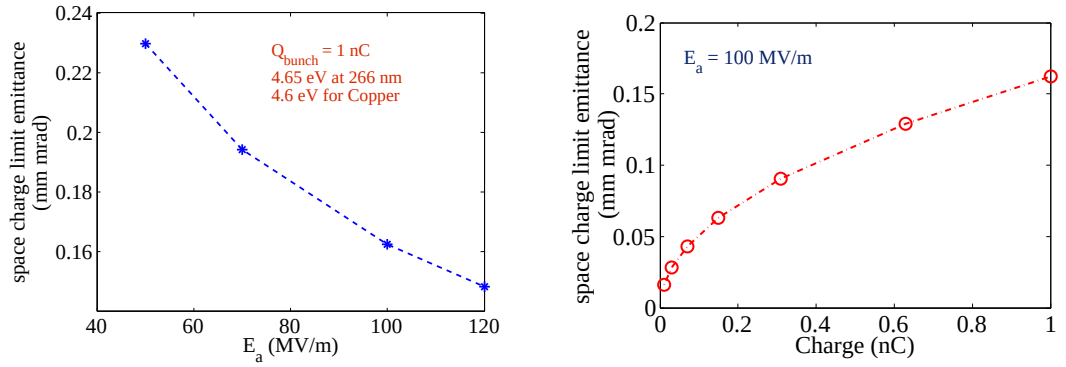

(a) **(b)**

Fig. 3: Space-charge limit emittance as function of a) the applied field at and b) the charge for a Cu cathode (Φ_{eff}=4.6 eV), illuminated by a UV laser pulse ($\hbar\omega = 4.66$ eV at 266 nm).

These modes are the transverse magnetic or $\text{TM}_{m,n,p}$ modes, since $B_z = 0$ and m, n, and p denote the rotational symmetry, the radial dependence, and the longitudinal mode of the cavity, respectively. In particular, the m-mode number represents the azimuthal angle, defining the ϑ-dependence or rotational symmetry of the fields. For all RF guns, since a beam with rotational symmetry is desired, $m = 0$. The p-mode number denotes the longitudinal mode of cavity, contributing to the RF emittance; for this reason, the full cell length for most RF guns is $\lambda/2$ and $p = 1$.

Considering a pillbox geometry for the RF gun cavity, the longitudinal electric field is

$$E_z^{mnp}(r,z) = E_0 J_m(k_{mn} r)\cos(m\vartheta)\cos\left(\frac{2p\pi z}{\lambda}\right)\mathrm{e}^{\mathrm{i}\omega z/c}\,, \tag{21}$$

with $J_m(k_{mn}r)$ the mth-order Bessel function, k_{mn} the nth zero of the mth-order Bessel function. Considering the π-mode for a $1^{1/2}$-cell standing wave RF structure, therefore, $m = 0$, $n = 0$, $p = 1$, and the gun longitudinal field is $E_z = E_0\cos(kz)\sin(\omega t + \phi_0)$, presenting the maximum field on the cathode surface, i.e., at $z = 0$ ($k = \omega/c$, with ω the RF angular frequency, and ϕ_0 the RF phase at which electrons leave the cathode surface and start to be accelerated). The radial field E_r and the azimuthal field B_ϑ can be derived by solving the Maxwell equations:

$$E_r = \frac{kr}{2}E_0\sin(kz)\sin(\omega t+\phi_0) = -\frac{r}{2}\frac{\partial}{\partial z}E_z\,, \tag{22}$$

$$B_\vartheta = c\frac{kr}{2}E_0\cos(kz)\cos(\omega t+\phi_0) = \frac{r}{2c}\frac{\partial}{\partial t}E_z\,, \tag{23}$$

where $k = 2\pi/\lambda$ is the RF wave number.

The force acting on a particle in the RF gun can be derived by combining E_r and B_ϑ:

$$F = e(E_r - \beta c B_\vartheta)\,. \tag{24}$$

The radial momentum kick is obtained by integrating the radial force impulse over the position at the last iris:

$$\Delta p_r = e\int E_r\frac{\mathrm{d}z}{\beta c} = -\frac{e}{2}\int\frac{r}{\beta c}\frac{\partial E_z}{\partial z}\mathrm{d}z\,. \tag{25}$$

Assuming that the RF field is a constant step function over the gun length, the change in radial momentum is

$$\Delta p_r = -\frac{eE_0}{m_0c^2}r\sin\phi, \tag{26}$$

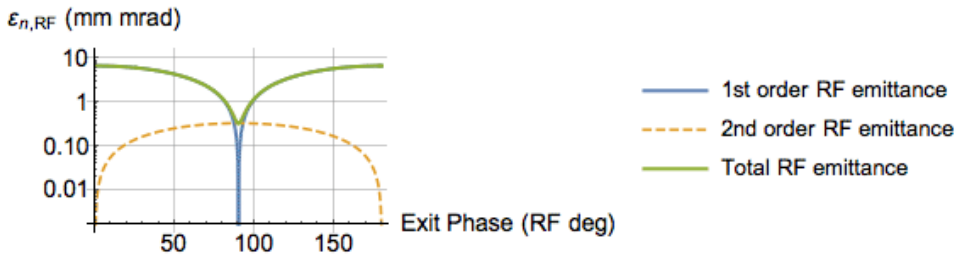

Fig. 4: RF emittance as a function of the exit phase for a 100 MV/ m gun with a 1 mm r.m.s. size beam and a Gaussian longitudinal distribution of 4 RF degrees r.m.s. at the exit iris, corresponding to a 10 ps FWHM bunch length. The total emittance (green solid line) is the quadratic sum of the first-order (blue solid line) and second-order (orange dashed line) emittances.

which depends on the applied field and the phase with respect to the wave, therefore, on the relative position of the particle within the bunch. Moving from cylindrical to Cartesian co-ordinates, we obtain the change in transverse momentum at the exit of the iris in terms of a kick angle x':

$$\Delta p_x = \beta\gamma x' = -\frac{eE_0}{2m_0c^2} x \sin\phi \qquad \rightarrow \qquad x' = -\frac{eE_0}{2\beta\gamma m_0c^2} x \sin\phi. \tag{27}$$

The RF gun can then be schematized as a defocusing lens: the electron exiting the gun undergoes a transverse kick from the exit iris, which can be written in terms of a focal length, f_{RF}:

$$x' = \frac{x}{f_{\mathrm{RF}}} \qquad \rightarrow \qquad f_{\mathrm{RF}} = -\frac{2\beta\gamma m_0c^2}{eE_0 \sin\phi}\,. \tag{28}$$

The focal strength is phase dependent, therefore electrons at different longitudinal positions, or slices, along the bunch, arriving at different phases at the gun exit, experience different kicks. In numbers (a SPARC_LAB case), an S-band standing wave RF gun operating at $E_0 = 110$ MV/ m, $\phi = 30°$, and an electron energy of 5 MeV, has a focal length $f_{\mathrm{RF}} = -18$ cm, where the minus sign denotes the defocusing effect of the gun exit iris. The different angular kicks received by the different slices along the bunch contribute to an increase in the overall projected emittance, which can be estimated by deriving the r.m.s. divergence from the variation of the angular dispersion with the exit phase, as

$$\Delta x' = -\frac{\mathrm{d}}{\mathrm{d}\phi}\left(\frac{1}{f_{\mathrm{RF}}}\right)\Delta x \Delta\phi\,, \tag{29}$$

and averaging over the particle distribution we get

$$\sigma_{x'} = \frac{eE_0 \cos\phi}{2\gamma m_0c^2}\sigma_x\sigma_\phi\,. \tag{30}$$

The impact of the phase dependence on the projected emittance is then summarized as

$$\varepsilon_{\mathrm{n}}^{\mathrm{RF}} = \frac{eE_0}{2m_0c^2}\sigma_x^2\sigma_\phi\sqrt{\cos^2\phi + \frac{\sigma_\phi^2}{2}\sin^2\phi}\,, \tag{31}$$

as shown in Fig. 4. At 90°, corresponding to the crest of the RF field, the phase space is strongly correlated; this means that all the slices lie on the same line, resulting in a minimum in the total RF emittance; conversely, far from the crest, each slice in the bunch explores more different fields, though contributing with a different slice emittance, resulting in a finite projected RF emittance.

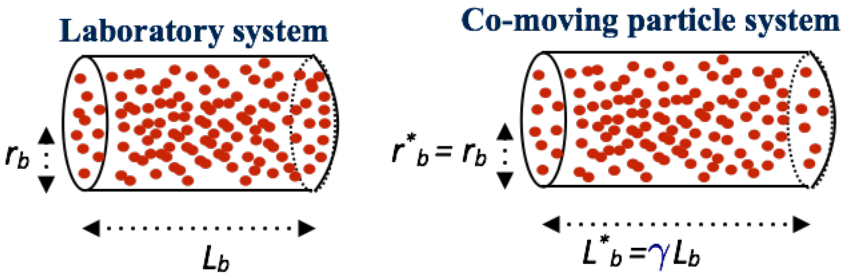

Fig. 5: Cylindrical bunch distribution in both the laboratory and the co-moving particle frame

4.2.1 Space-charge derivation

Space-charge forces influence the beam dynamics and are one of the main performance limitations in high-brightness photo-injectors.

To describe the origin of space-charge forces, let us consider the case of highly relativistic bunches (Fig. 5). In the laboratory system, let us assume N relativistic electrons uniformly distributed in a cylinder with radius r_b and length L_b; in a co-moving particle co-ordinate system, electrons are at rest and the field is a pure Coulomb field. When transforming from the laboratory frame to the co-moving one, the number of electrons and the radius remain invariant, while the length is expanded by a factor γ, the Lorentz factor. Therefore, since $\gamma \gg 1$, the approximation of an infinitely long cylindrical distribution is valid and, by applying the Gauss theorem, the electric field is retrieved having only a radial component:

$$E^*_r(r) = -\frac{Ne}{2\pi\varepsilon_0 L^*_\mathrm{b}}\frac{r}{r^2_\mathrm{b}}\,, \qquad r \le r_\mathrm{b}\,, \tag{32}$$

$$E^*_r(r) = -\frac{Ne}{2\pi\varepsilon_0 L^*_\mathrm{b}}\frac{1}{r}\,, \qquad r \ge r_\mathrm{b}\,. \tag{33}$$

Transforming back to the laboratory frame, the radial component of the electric field yields a radial electric field and an azimuthal magnetic field [45]:

$$E_r(r) = \gamma E^*_r(r) = -\frac{Ne}{2\pi\varepsilon_0 L_\mathrm{b}}\frac{r}{r^2_\mathrm{b}}\,, \tag{34}$$

$$B_\phi(r) = \frac{v}{c^2}E_r(r)\,, \qquad r \le r_\mathrm{b}\,. \tag{35}$$

The force a test particle inside the bunch experiences due to E_r and B_ϕ is given by the Lorentz force, $\vec{F} = -e(\vec{E} + \vec{v} \times \vec{B})$; therefore,

$$F_r(r) = \frac{Ne^2}{2\pi\varepsilon_0 L_\mathrm{b}}\frac{r}{r^2_\mathrm{b}}\left(1 - \frac{v^2}{c^2}\right) = \frac{Ne^2}{2\pi\varepsilon_0 L_\mathrm{b}}\frac{r}{r^2_\mathrm{b}}\frac{1}{\gamma^2}\,, \tag{36}$$

which has a linear dependence on r and is proportional to γ^{-2}. The overall force points outwards and is then a defocusing force, which vanishes for $\gamma \to \infty$.

The repulsive space-charge forces represent an unavoidable issue, which must be compensated to avoid a strong increase in emittance. For cylindrical bunch transverse distributions, the total space-charge force depends linearly on the displacement r, as shown in Eq. (36). The linear dependence on the particle displacement from the axis produces a quasi-laminar propagation of the beam, since there is a full correlation between the particles' position and their transverse angle; the particle motion follows a laminar flow, therefore, particle trajectories do not cross each other. Therefore, applying a magnetic lens, such as a solenoid, whose field increases linearly with r, the internal forces are counterbalanced and the beam is focused, contributing to preserve the emittance.

In the case of Gaussian transverse beam distribution, the radial force does not depend linearly on r, as

$$F_r(r) = \frac{Ne^2}{2\pi\varepsilon_0 L_\mathrm{b} r}\left(1 - \mathrm{e}^{-\frac{r^2}{2\sigma^2}}\right)\frac{1}{\gamma^2}\,: \tag{37}$$

it increases almost linearly from the axis ($r = 0$) up to 0.8σ of the Gaussian distribution, then it reverses its trend and starts decreasing for $r > 1.8\sigma$, since the charge density is lower than around the axis. In this case, space-charge forces cannot be fully compensated. A flat, uniform beam distribution is also advantageous in the longitudinal direction, because slices in the core or in the tails would have different charge density otherwise, experiencing a different defocusing effect due to space-charge along the bunch, while the same external focusing force is applied along the bunch.

4.3 Emittance compensation

In the 1980s, Carlsten [46] first explained how to reduce the emittance increase induced by space-charge in a RF gun. He suggested using a solenoid, placed at the exit of the RF gun, to control the emittance oscillations in the downstream drift.

The beam can be virtually divided, in the longitudinal direction, by thin slices, each having its own transverse phase space distribution. Assuming that each slices are independent and do not interact with each other, the projected emittance is the phase space ellipse, which encloses all the slice phase space. At the cathode, all the slices have low angular divergence and they can be considered almost aligned, resulting in a projected emittance which is close to the intrinsic one. As the beam leaves the cathode surface, the slices undergo different angular kicks, depending on their peak current. The ensemble of phase spaces of each slice forms a kind of fan, resulting in a larger enclosing ellipse and, therefore, in an increased projected emittance. A solenoid, whose focusing field is linear, can be used to give to each slice a kick of the same sign. Indeed, the beam entering the end radial field of the solenoid receives a transverse kick and rotates inward or outward, depending on the solenoid polarity. The particle is then closer in when passing through the end radial field at the opposite end of the solenoid and, since it is further in, the kick is smaller. After the solenoid, the beam drifts a distance with the slices all converging at a beam waist, placed at the entrance of the high-energy linac. To prevent additional space-charge emittance increase in subsequent accelerating sections, the final emittance minimum has to be reached at high beam energy so that space-charge forces are sufficiently damped. Indeed, the linac boosts the beam energy from the space-charge-dominated regime to the emittance-dominated one, freezing the aligned slices. Therefore, a solenoidal field is needed to focus the beam and match it into a high-gradient booster to damp emittance oscillations.

In the space-charge-dominated regime, i.e., when the space-charge collective force is largely dominant over the emittance pressure, mismatches between the space-charge correlated forces and the external RF focusing gradient produce slice envelope oscillations that cause normalized emittance oscillations, also referred to as plasma oscillations.[2] It has been shown [48] that to conveniently damp emittance oscillations the beam has to be injected into the booster with a laminar envelope waist and the booster accelerating gradient has to be properly matched to the beam size, energy, and peak current, according to

$$\gamma' = \frac{2}{\sigma}\sqrt{\frac{I_\mathrm{p}}{2I_\mathrm{A}\gamma}}\,, \tag{38}$$

with $\gamma' \approx 2E_\mathrm{acc}$, where E_acc is the accelerating field. The matching condition guarantees emittance oscillation damping, preserving beam laminarity during acceleration. The final value of the emittance, however, is strongly dependent on the phase of the plasma oscillation at the entrance of the booster, whose typical behaviour is shown in Fig. 6, as computed by numerical simulations with PARMELA code [49] for different initial electron pulse shapes, i.e., flat top with different rise time from a pure cylindrical

[2] For further detailed studies refer to Ref. [47].

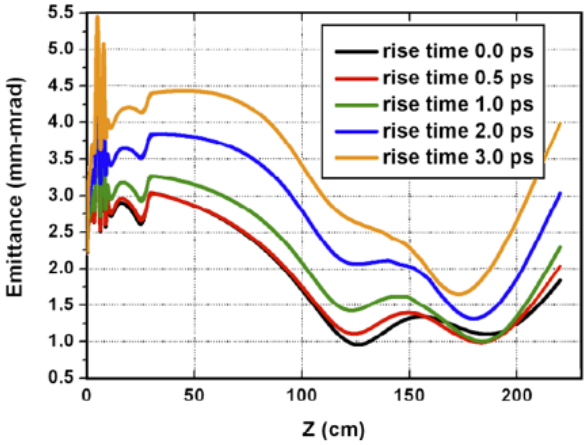

Fig. 6: Normalized r.m.s. emittance oscillations in the drift downstream the RF gun as computed by PARMELA, for different initial electron pulse rise times. Gun length, 15 cm, solenoid length 20 cm centred at z = 20 cm [52].

bunch (0 ps rise time) to a quasi-Gaussian distribution (3 ps rise time). The emittance minimum decreases for shorter rise times because of the reduced non-linear transverse space-charge effects in cylindrical-like bunch charge distributions [50]. In addition, an emittance oscillation appears in the drift downstream of the RF gun, showing a double emittance minimum [51]. The relative emittance maximum disappears at longer rise times and becomes a 'knee' in a quasi-Gaussian distribution (yellow curve in Fig. 6). Emittance oscillations of this kind are produced by a beating between head and tail plasma frequencies caused by correlated chromatic effects in the solenoid. The working point matching condition, suitable for damping emittance oscillations, requires the emittance to be a local maximum and the envelope to be a waist at the entrance to the booster. In this way, the second emittance minimum can be shifted at higher energies and frozen at the smallest value, taking advantage of the additional emittance compensation occurring in the booster. The waist size is related to the strength of the RF fields and the peak current: RF focusing aligns the slices, resulting in a smaller projected emittance, and acceleration damps the emittance oscillations.

Experimental evidence of emittance oscillations in the drift before the booster has been obtained at the SPARC high-brightness photo-injector [52] by using an emittance meter [53] to measure the evolution of the beam transverse phase space in the drift downstream of the RF gun. The behaviour of both projected normalized emittance and envelope along the longitudinal co-ordinate z is reported in Fig. 7. The projected emittance evolution along z shows the expected double minimum oscillation, which is crucial in achieving minimum emittance in high-brightness photo-injectors.

4.4 Longitudinal compression

Space-charge effects at low energy prevent the generation of short, subpicosecond, electron bunches, with a significant amount of charge (tens of picocoulombs) directly from the electron source, leading to emittance degradation and bunch elongation within a few centimetres downstream of the cathode. Bunch compression is therefore necessary to shorten the electron pulse, achieving a high peak current, of the order of kiloamps. Either magnetic or RF-based compression methods can be used for this purpose.

In magnetic compressors, a bunch with a time-energy correlation (or chirp) is driven along an energy-dependent path length by a dispersive, non-isochronous beam transport section [54]. While this scheme has been proved successful in increasing the beam current at high energies, the emittance increase due to coherent synchrotron radiation in bending magnets can be dramatic. As an alternative, the compression scheme used at SPARC_LAB exploits the interaction with the electromagnetic fields of an accelerating cavity. Based on RF compression, it uses rectilinear trajectories, avoiding the degradation

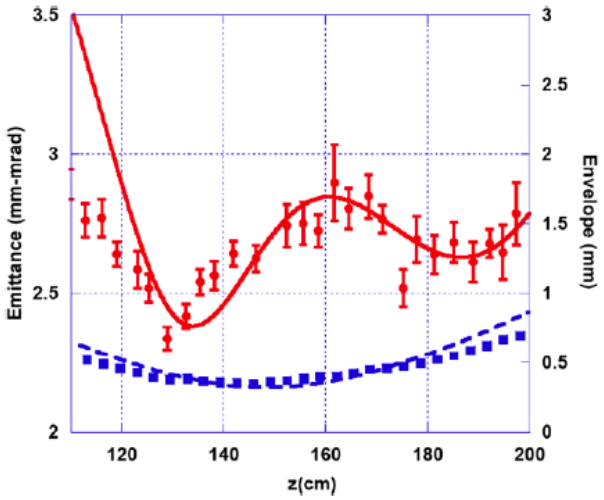

Fig. 7: Normalized emittance and envelope (r.m.s. values) evolution from the cathode up to the beam line end, as computed by PARMELA (red and blue curves), compared with measurements (red dots and blue squares) taken in the emittance meter range (up to 2 m from the cathode). Beam measured parameters: 500 pC, 5 ps FWHM (quasi-flat top pulse shape), 1.5 ps rise time, 5 MeV.

due to coherent synchrotron radiation suffered by the beam going through bending trajectories. In addition, working at relatively low energy [55], of the order of megaelectronvolts, it can be integrated into the emittance compensation process [46] illustrated in the previous section. This scheme is commonly known as *velocity bunching* [56].

The longitudinal phase space rotation in the velocity-bunching process is based on a correlated time-velocity chirp in the electron bunch, causing electrons in the bunch tail to be faster than electrons in the bunch head. The correlated chirp induces a longitudinal phase space rotation in the travelling RF wave potential (longitudinal focusing), accelerating the beam inside a long multicell RF structure, as depicted in Fig. 8 (right panel).[3] Thus, simultaneously, an of-crest energy chirp is applied to the injected beam. Subrelativistic electrons injected into a travelling wave cavity at zero crossing field phase move more slowly than the RF wave. Thus, the beam slips back to phases, towards $-90°$, as shown in Fig. 8 (left-hand panel), where the field is accelerating, and it is chirped and compressed: compression and acceleration take place at the same time within the same accelerating section, i.e., the first one following the RF gun. The velocity-bunching technique is characterized by longitudinal and transverse phase space distortions, leading to asymmetric current profiles and higher final projected emittances, which can, however, be minimized by keeping the transverse beam size under control through solenoidal magnetic fields in the region where the bunch is undergoing compression and the electron density is increasing [57]. For this reason, the typical layout for a high-brightness RF photo-injector, shown in Fig. 2, presents solenoid coils embedding the first two accelerating sections. As shown in Fig. 9, the effect on emittance compensation produced by the solenoids is clearly visible in the simulation (right plot: curve c).

5 Conclusions

High-brightness electron beams can be achieved in RF photo-injectors by means of RF guns, equipped with laser-driven photocathodes, followed by booster sections. An emittance compensation scheme [46] based on a focusing solenoid at the exit of the RF gun can be used in photo-injectors to control emittance increase due to space-charge effects. In addition, by properly matching the transverse phase space of the electron beam with the downstream accelerating sections (booster), it is possible to control the transverse

[3] General Particle Tracer is a 3D code to study charged-particle dynamics in electromagnetic fields.

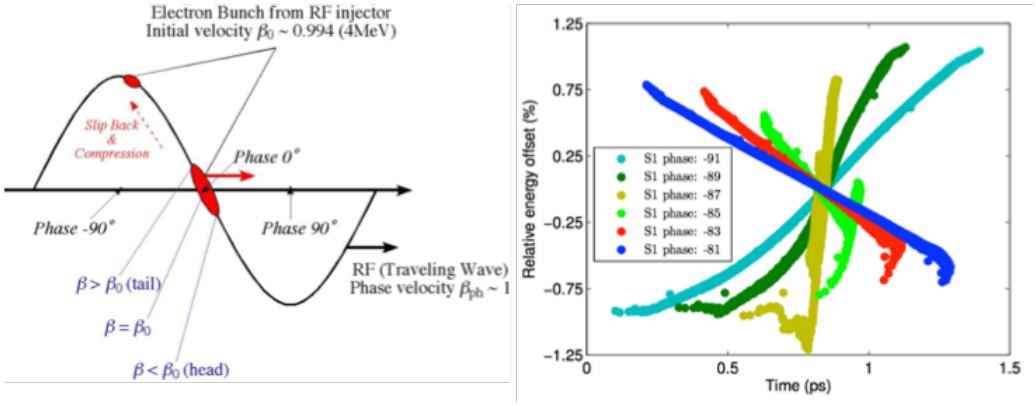

Fig. 8: Left-hand side: longitudinal electric field in the first travelling wave section as a function of RF phase, showing slippage of the beam, injected at the 0 crossing phase, towards $-90°$. Right-hand side: General Particle Tracer simulation of the longitudinal phase space. The maximum bunch compression, for this case, occurs at around $-87°$ (olive green curve).

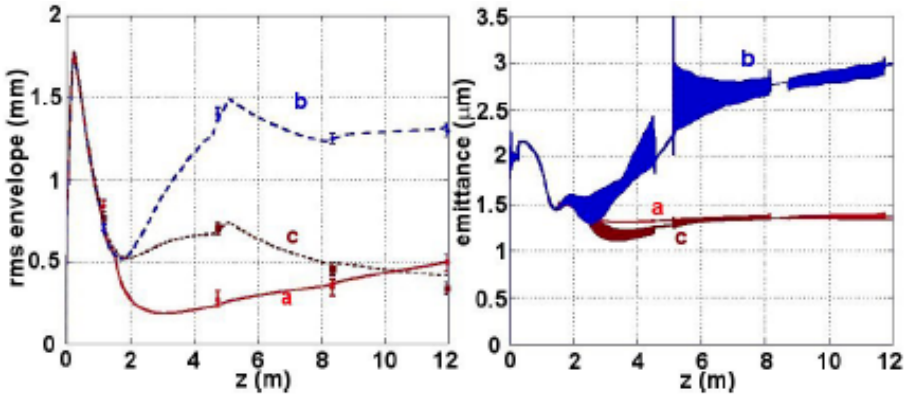

Fig. 9: Left-hand side: measured envelopes and PARMELA simulations. Right-hand side: emittance evolution along the linac (PARMELA simulations); (a) no compression, (b) compression with solenoids off along the first travelling wave section, (c) same compression with solenoids set to 450 G [57].

emittance oscillations during the acceleration. Under conditions of invariant envelope and proper phasing of space-charge oscillations [52], the final emittance is almost compensated down to the intrinsic emittance value given by cathode emission, with an expected emittance scaling such as $\varepsilon_{\rm n} \sim \sigma_{\rm cathode} \sim \sqrt{Q}$, where $\sigma_{\rm cathode}$ is the hitting laser spot size on the photocathode, and Q is the extracted electron charge. A compression stage can occur to shorten the beam length so to achieve the required large peak current. The so-called velocity-bunching method [55] has opened up a new possibility of compressing the beam inside an RF structure and, if integrated in the emittance compensation process [48, 56], can provide the desired bunch current values with the advantage of compactness of the machine and absence of the coherent synchrotron radiation effects present in a magnetic compressor [58–60]. It is interesting to note that a shortened beam length also enables the energy spread dilution due to RF curvature degradation to be contained; indeed the energy spread depends on the bunch length and the accelerating frequency as $\Delta\gamma/\gamma \approx 2((\pi f_{\rm RF}\sigma_z)/c)^2$, where an on-crest operation, in full relativistic conditions, has been considered.

The electron source is one of the key components, since the brightness generated at the electron source represents the ultimate achievable value. The final application must drive the choice of both electron source and injector, since stability and reliability are common issues. Photo-injectors have the advantage of producing a variety of bunch trains that can be tailored to the needs of a particular machine

by properly shaping the laser pulses. Photocathodes (with respect to thermionic sources) can easily produce peak current densities of the order of kiloamps per centimetre squared, and high current densities at the cathode are needed to minimize the transverse emittance. Conversely, DC photocathode electron guns are the best solution for high-average power beams.

Acknowledgements

The material for this lecture has been liberally taken from talks, papers, lectures, proceedings, and notes from a large number of people, whom I acknowledge here. References are listed in the text: S. Di Mitri, D.H. Dowell, D. Filippetto, P. Musumeci, F. Sannibale. In addition, I wish to thank M. Ferrario, A. Cianchi, and A. Mostacci for helpful discussions, suggestions, and revision.

References

[1] C. Bostedt *et al.*, *Rev. Mod. Phys.* **88** (2016) 015007, https://doi.org/10.1103/RevModPhys.88.015007.

[2] V. Ayvazyan *et al.*, *Phys. Rev. Lett.* **88** (2002) 104802, https://doi.org/10.1103/PhysRevLett.88.104802.

[3] W. Ackermann *et al.*, *Nat. Photonics* **1** (2007) 336, https://doi.org/10.1038/nphoton.2007.76.

[4] C.J. Bocchetta *et al.*, Conceptual design report for the FERMI@Elettra project, ST/F-TN-07/12 (2007).

[5] M. Tigner, *Il Nuovo Cimento* **37** (1965) 1228, https://doi.org/10.1007/BF02773204.

[6] `http://www.eli-np.ro/documents/ELI-NP-WhiteBook.pdf`, last accessed December 06th 2017.

[7] P.A. Walker *et al.*, *J. Phys. Conf. Ser.* **874** (2017) 012029, https://doi.org/10.1088/1742-6596/874/1/012029.

[8] C. Lejeune and J. Aubert, *Adv. Electron. Electron Phys., Suppl. A* **13** (1980) 159.

[9] A.W. Chao and M. Tigner, *Handbook of Accelerator Physics and Engineering* (World Scientific, Singapore, 2013), p. 255, https://doi.org/10.1142/8543.

[10] C.A. Brau, in *The Physics and Applications of High Brightness Electron Beams*, Eds. J. Rosenzweig *et al.* (World Scientific, Singapore, 2003), p. 20, https://doi.org/10.1142/9789812705235_0002.

[11] M. Reiser, *Theory and Design of Charged Particle Beams* (Wiley-VCH, Weinheim, 2008), p. 61, https://doi.org/10.1002/9783527622047.

[12] Shyh-Yuan Lee, *Accelerator Physics* (World Scientific, Singapore, 2011), p. 419.

[13] J. Clarke, *The Science and Technology of Undulators and Wigglers* (Oxford University Press, Oxford), p. 73.

[14] R. Bonifacio *et al.*, *Opt. Commun.* **50** (1984) 373, https://doi.org/10.1016/0030-4018(84)90105-6.

[15] J.S. Fraser *et al.*, *Nucl. Instrum. Methods Phys. Res. A* **250** (1986) 71, https://doi.org/10.1016/0168-9002(86)90862-4.

[16] F. Villa *et al.*, *Nucl. Instrum. Methods Phys. Res. A* **829** (2016) 446, https://doi.org/10.1016/j.nima.2016.01.010.

[17] P. Chen *et al.*, *Phys. Rev. Lett.* **54** (1985) 693, https://doi.org/10.1103/PhysRevLett.54.693.

[18] F. Giorgianni *et al.*, *Appl. Sci.* **6** (2016) 2, https://doi.org/10.3390/app6020056.

[19] V. Petrillo *et al.*, *Phys. Rev. Lett.* **111** (2013) 114802, https://doi.org/10.1103/PhysRevLett.111.114802.

[20] A.A. Lutman *et al.*, *Phys. Rev. Lett.* **110** (2013) 134801, https://doi.org/10.1103/PhysRevLett.110.134801.

[21] G. De Ninno *et al.*, *Phys. Rev. Lett.* **110** (2013) 064801, https://doi.org/10.1103/PhysRevLett.110.064801.

[22] W. Anders *et al.*, in *An Engineering Guide to Photo-injectors*, Eds. D.H. Dowell and T. Rao, p. 271, CreateSpace Independent Publishing Platform (April 2, 2013).

[23] B. Von Borries and E. Rushka, *Z. Tech. Phys.* **20** (1939) 225.

[24] O. J. Luiten *et al.*, Ultracold electron sources, Proc. 46th Workshop of the INFN Eloisatron Project, Erice, 2005.

[25] C. Herring and M.H. Nichols, *Rev. Mod. Phys.* **21** (1949) 185, https://doi.org/10.1103/RevModPhys.21.185.

[26] P.G. O'Shea *et al.*, *Nucl. Instrum. Methods Phys. Res. A* **318** (1992) 52, https://doi.org/10.1016/0168-9002(92)91023-3.

[27] K.C.D. Chan *et al.*, *Nucl. Instrum. Methods Phys. Res. A* **318** (1992) 148, https://doi.org/10.1016/0168-9002(92)91041-7.

[28] M. Ferrario *et al.*, *Nucl. Instrum. Methods Phys. Res. B* **309** (2013) 183, https://doi.org/10.1016/j.nimb.2013.03.049.

[29] A. R. Rossi *et al.*, *Physics Procedia* **52** (2014) 90, https://doi.org/10.1016/j.phpro.2014.06.014.

[30] P. Schmüser *et al.*, *Ultraviolet and Soft X-ray Free Electron Lasers* (Springer, Berlin, 2008).

[31] H. Alfvén, *Phys. Rev.* **55** (1939) 425, https://doi.org/10.1103/PhysRev.55.425.

[32] J.D. Lawson, *J. Electron. Control* **5** (1958) 146, https://doi.org/10.1080/00207215808953898.

[33] C. Curatolo *et al.*, *Phys. Rev. Accel. Beams* **20** (2017) 080701, https://doi.org/10.1103/PhysRevAccelBeams.20.080701.

[34] I. Blumenfeld *et al.*, *Phys. Rev. ST Accel. Beams* **13** (2010) 111301, https://doi.org/10.1103/PhysRevSTAB.13.111301.

[35] T. Ishikawa *et al.*, *Nat. Photonics* **6** (2012) 540, https://doi.org/10.1038/nphoton.2012.141.

[36] T. Asaka *et al.*, *Phys. Rev. Accel. Beams* **20** (2017) 080702, https://doi.org/10.1103/PhysRevAccelBeams.20.080702.

[37] S. Di Mitri and M. Cornacchia, *Phys. Rep.* **539** (2014) 1, https://doi.org/10.1016/j.physrep.2014.01.005.

[38] E.L. Murphy and R.H. Good, *Phys. Rev.* **102** (1956) 1464, https://doi.org/10.1103/PhysRev.102.1464.

[39] L.A. Dubridge, *Phys. Rev.* **43** (1933) 0727, https://doi.org/10.1103/PhysRev.43.727.

[40] V. Fusco *et al.*, Spatial autocorrelation for transverse beam quality characterization, Proc. EPAC08, TUPC027, Genova, Italy (2008).

[41] L.W. Nordheim, *Proc. R. Soc. Lond. A* **121** (1928) 626, https://doi.org/10.1098/rspa.1928.0222.

[42] D.H. Dowell *et al.*, *Phys. Rev. ST Accel. Beams* **9** (2006) 063502, https://doi.org/10.1103/PhysRevSTAB.9.063502.

[43] P. Musumeci *et al.*, *Phys. Rev. Lett.* **104** (2010) 084801, https://doi.org/10.1103/PhysRevLett.104.084801.

[44] D. Filippetto *et al.*, *Phys. Rev. ST Accel. Beams* **17** (2014) 024201, https://doi.org/10.1103/PhysRevSTAB.17.024201.

[45] J.D. Jackson *Classical Electrodynamics*, 3rd ed. (Wiley, New York, 1999).

[46] B.E. Carlsten, *Nucl. Instrum. Methods Phys. Res. A* **285** (1989) 313, https://doi.org/10.1016/0168-9002(89)90472-5.

[47] M. Ferrario, Space charge mitigation, Proc. CERN Accelerator School: Free Electron Lasers and Energy Recovery Linacs, Hamburg, Germany, 2016.

[48] L. Serafini and J.B. Rosenzweig, *Phys. Rev. E* **55** (1997) 7565,

https://doi.org/10.1103/PhysRevE.55.7565.

[49] L.M. Young, LANL Report LA-UR-96-1835.

[50] J. Yang *et al.*, *J. Appl. Phys.* **92** (2002) 1608, https://doi.org/10.1063/1.1487457.

[51] M. Ferrario *et al.*, SLAC, Report SLAC-PUB-8400.

[52] M. Ferrario *et al.*, *Phys. Rev. Lett.* **99** (2007) 234801, https://doi.org/10.1103/PhysRevLett.99.234801.

[53] A. Cianchi *et al.*, *Phys. Rev. ST Accel. Beams* **11** (2008) 032801, https://doi.org/10.1103/PhysRevSTAB.11.032801.

[54] S. Di Mitri, Bunch length compressors, Proc. CERN Accelerator School: Free Electron Lasers and Energy Recovery Linacs, Hamburg, Germany, 2016.

[55] B. Aune and R.H. Miller, Report SLAC-PUB 2393, 1979.

[56] L. Serafini and M. Ferrario, *AIP Conf. Proc.* **581** (2001) 87, https://doi.org/10.1063/1.1401564.

[57] M. Ferrario *et al.*, *Phys. Rev. Lett.* **104** (2010) 054801, https://doi.org/10.1103/PhysRevLett.104.054801.

[58] P. Emma, Accelerator physics challenges of X-ray FEL SASE sources, Proc. EPAC2002, (Paris, France, 2002).

[59] L.I. Schiff, *Rev. Sci. Instr.* **17** (1946) 6, https://doi.org/10.1063/1.1770395.

[60] M. Dohlus and T. Limberg, Emittance growth due to wake fields on curved bunch trajectories, XVIII International Free Electron Laser Conf., 'Rome, Italy, 1996.